

# Toward High Efficiency Water Processed Organic Photovoltaics: Controlling the Nanoparticle Morphology with Surface Energies

Hugo Laval, Alexandre Holmes, Matthew A. Marcus, Benjamin Watts, Gwenaël Bonfante, Marc Schmutz, Elise Deniau, Robin Szymanski, Christine Lartigau-Dagron, Xiaoxue Xu, Julie M. Cairney, Kazuhiko Hirakawa, Fumiyasu Awai, Takaya Kubo, Guillaume Wantz, Antoine Bousquet,\* Natalie P. Holmes,\* and Sylvain Chambon\*

Here efficient organic photovoltaic devices fabricated from water-based colloidal dispersions with donor:acceptor composite nanoparticles achieving up to 9.98% power conversion efficiency (PCE) are reported. This high efficiency for water processed organic solar cells is attributed to morphology control by surface energy matching between the donor and the acceptor materials. Indeed, due to a low interfacial energy between donor and the acceptor, no large phase separation occurs during the nanoparticle formation process as well as upon thermal annealing. Indeed, synchrotron-based scanning transmission X-ray microscopy reveals that the internal morphology of composite nanoparticles is intermixed as well as the active layer morphology after thermal treatment. The PCE of this system reaches 85% that of devices prepared from chlorinated solvent. The gap between water-based inks and organic solvent-based inks gets narrower, which is promising for the development of eco-friendly processing and fabrication of organic photovoltaics.

## 1. Introduction

Organic photovoltaics (OPV) are becoming a credible solar conversion technology as power conversion efficiencies (PCEs) are constantly increasing and the operational stability is improving. In particular, non-fullerene acceptors (NFA) have been a game changer in the field, since this class of organic semiconductors has overcome some of the inherent limitations of the fullerene derivatives used for decades in OPV. First, NFA have a broad and tunable absorption which can be complementary to the donor material.<sup>[1]</sup> They can also present lower voltage loss<sup>[2,3]</sup> and higher stability than fullerene derivatives.<sup>[1,4]</sup> Due to these advantages, the PCE in OPV field

H. Laval, R. Szymanski, G. Wantz, S. Chambon  
 Univ. Bordeaux  
 CNRS  
 Bordeaux INP  
 IMS  
 UMR 5218, Talence F-33400, France  
 E-mail: sylvain.chambon@ims-bordeaux.fr  
 A. Holmes, E. Deniau, C. Lartigau-Dagron, A. Bousquet  
 Université de Pau et des Pays de l'Adour  
 E2S UPPA  
 CNRS  
 IPREM  
 Pau 64043, France  
 E-mail: antoine.bousquet@univ-pau.fr

M. A. Marcus  
 Advanced Light Source  
 Lawrence Berkeley National Laboratory  
 Berkeley, CA 94720, USA  
 B. Watts  
 Paul Scherrer Institute  
 Villigen-PSI 5232, Switzerland  
 G. Bonfante, K. Hirakawa, S. Chambon  
 LIMMS/CNRS-IIS (IRL2820)  
 Institute of Industrial Science  
 The University of Tokyo  
 4-6-1 Komaba, Meguro-ku, Tokyo 153-8505, Japan  
 M. Schmutz  
 Université de Strasbourg  
 CNRS  
 Institut Charles Sadron-UPR22  
 rue du Loess Strasbourg, Strasbourg 67034, France  
 E. Deniau  
 Institut des Molécules et Matériaux du Mans  
 UMR CNRS 6283  
 Le Mans Université  
 Le Mans Cedex 9, Le Mans 72085, France  
 X. Xu  
 School of Biomedical Engineering  
 Faculty of Engineering and Information Technology  
 University of Technology Sydney  
 Sydney, New South Wales 2007, Australia

 The ORCID identification number(s) for the author(s) of this article can be found under <https://doi.org/10.1002/aenm.202300249>

© 2023 The Authors. Advanced Energy Materials published by Wiley-VCH GmbH. This is an open access article under the terms of the Creative Commons Attribution License, which permits use, distribution and reproduction in any medium, provided the original work is properly cited.

DOI: 10.1002/aenm.202300249

has increased drastically in the last years, now reaching 19%.<sup>[5,6]</sup> OPV also have a low energy pay-back time due to low temperature processes<sup>[7,8]</sup> allowing for the possibility to develop light-weight and semi-transparent modules.<sup>[9]</sup> These advantages make this technology amenable to building integrated photovoltaic,<sup>[9]</sup> outdoor,<sup>[10]</sup> and indoor applications.<sup>[11]</sup>

In the process of fabrication of OPV devices, the organic semiconductors, a donor and an acceptor material, are usually dissolved in an organic solvent and deposited on substrates by various liquid-phase deposition techniques: spin-coating and doctor-blading for lab scale<sup>[12]</sup> processes or various roll-to-roll slot-die coating techniques for industrial development.<sup>[9]</sup> However, most solvents used for deposition are usually chlorinated and/or aromatic. They present high toxicity for the operators and the environment. Less-harmful solvents, such as xylene or tetrahydrofuran (THF), are sometimes used but still present acute toxicity.<sup>[13]</sup>

In order to render OPV technology to be more respectful of the environment, there is a need for minimizing the environmental impact of the overall process. Among the different solutions, aqueous dispersions appear to be the best to develop eco-friendly processes.<sup>[14]</sup> Over the years, two main strategies have been developed to fabricate water-based organic semiconductor inks: mini-emulsion<sup>[15,16]</sup> and nanoprecipitation.<sup>[17]</sup> The PCEs of devices fabricated from those colloidal inks have for a long time remained modest, below 1%.<sup>[18,19]</sup> Starting from 2013, interesting PCEs of 2% and 2.5% were achieved with the seminal work of Venkataraman and colleagues with poly(3-hexylthiophene-2,5-diyl) (P3HT):[6,6]-phenyl-C<sub>61</sub>-butyric acid methyl ester (PC<sub>61</sub>BM)<sup>[20]</sup> and Dastoor and colleagues with P3HT:indene-C60 bisadduct (ICBA),<sup>[21]</sup> respectively, and later on by D'Olieslaeger et al. with 3.8% reached using PBDTTPD:PC<sub>71</sub>BM nanoparticles.<sup>[22]</sup> However, the performances of OPV devices prepared from water-based dispersions were still lower than those which can be achieved with organic solvents. One of the reasons lies in the morphology achieved in polymer:fullerene composite nanoparticles (NP). Indeed, over the years, researchers have shown that due to high surface energy, the fullerene derivatives (PC<sub>61</sub>BM or ICBA) tend to migrate in the core of the nanoparticles during the nanoparticle formation using the mini-emulsion process.<sup>[21,23]</sup> Such morphology can provide a good charge separation.<sup>[24]</sup> However, it can

be detrimental to the performance of the devices, since charges may still be trapped in the core, leading to unbalanced charge transport. Thermal annealing can modify the morphology and nano-channels between the cores can be formed and improve the performances.<sup>[25]</sup> Nevertheless a more intimate morphology is desired for efficient OPV devices.

Nanoprecipitation gives rise to different types of morphology. Intermixed morphology is usually identified because of the fast nanoparticle formation process.<sup>[26]</sup> Recently, it has been shown that Janus nanoparticle morphology can also be achieved during nanoprecipitation.<sup>[27]</sup> Both morphologies are likely to be more adapted for organic photovoltaic applications. As a confirmation, Gärtner et al. first and Xie et al. later on, fabricated OPV devices with P3HT:ICBA nanoparticles in alcoholic dispersions and achieved 4% and 4.52% PCE, respectively. Very recently, Manger et al. achieved organic photovoltaic devices with up to 10.6% PCE using colloidal dispersion in acetonitrile.<sup>[28]</sup> On the water-based colloidal dispersion side, Xie et al. developed a surfactant (Pluronic F127) assisted nanoprecipitation method to generate organic semiconductor dispersed in water and reached up to 7.5% PCE with PBQ-QF:ITIC while devices with only 4.42% PCE were fabricated for mini-emulsion based dispersions.<sup>[29]</sup> More recently Xie et al. used the same surfactant assisted nanoprecipitation in water and applied it to the high efficiency donor/acceptor combination (PM6:BTP-eC9). They achieved 11% PCE but needed to use diiodooctane as additive.<sup>[30]</sup> Despite being highly effective, nanoprecipitation is more challenging to develop since it requires high solubility in THF and/or long dialysis procedure to increase the concentration to a sufficient level to reach appropriate active layers thicknesses, which is less desirable when moving the technology toward industrialization. Therefore, it is important to find solutions to control the morphology of composite nanoparticles during mini-emulsion processes in order to achieve high performances. In this quest, we have shown in a recent study dedicated to donor/acceptor composite nanoparticle morphology that the morphology is dependent on the surface energy difference between the donor and the acceptor.<sup>[31]</sup> Especially the morphology of donor/acceptor composite nanoparticles can be tuned by careful selection of the NFA. Indeed, fullerene derivatives-based donor/acceptor composite nanoparticles prepared by mini-emulsion present essentially core-shell morphology due to higher surface energy of the acceptor compared to that of the donor material. However, NFAs present lower surface energies than fullerene derivatives and, as a consequence, the morphology of donor/acceptor NP is not always acceptor-rich core/donor-rich shell. In particular, we have shown that some donor/acceptor systems such as TQ1:N2200, P3HT:N2200, and P3HT:eh-IDTBR can present donor-rich core/acceptor rich shell.<sup>[31]</sup> These findings show that it is possible to control the internal morphology of the nanoparticles by careful choice of the surface energies of both donor and acceptor.

Here we present the influence of the surface energy difference on the performances of organic solar cells fabricated from water-based colloidal dispersions. The donor conjugated polymer poly[(thiophene)-alt-(6,7-difluoro-2-(2-hexyldecyloxy)quinoxaline)] (PTQ10)<sup>[32]</sup> was associated with either PC<sub>61</sub>BM as acceptor or Y6, an NFA composed of a central core fused ring (dithienothiophen[3,2-b]-

J. M. Cairney, N. P. Holmes  
School of Aerospace, Mechanical and Mechatronic Engineering  
The University of Sydney  
Sydney, New South Wales 2006, Australia  
E-mail: natalie.holmes@sydney.edu.au

J. M. Cairney, N. P. Holmes  
Australian Centre for Microscopy and Microanalysis  
The University of Sydney  
Madsen Building F09, Sydney, New South Wales 2006, Australia

F. Awai, T. Kubo  
RCAST  
The University of Tokyo  
4-6-1 Komaba, Meguro-ku, Tokyo 153-8904, Japan

N. P. Holmes  
The University of Sydney Nano Institute  
Faculty of Science  
University of Sydney  
Sydney, New South Wales 2006, Australia

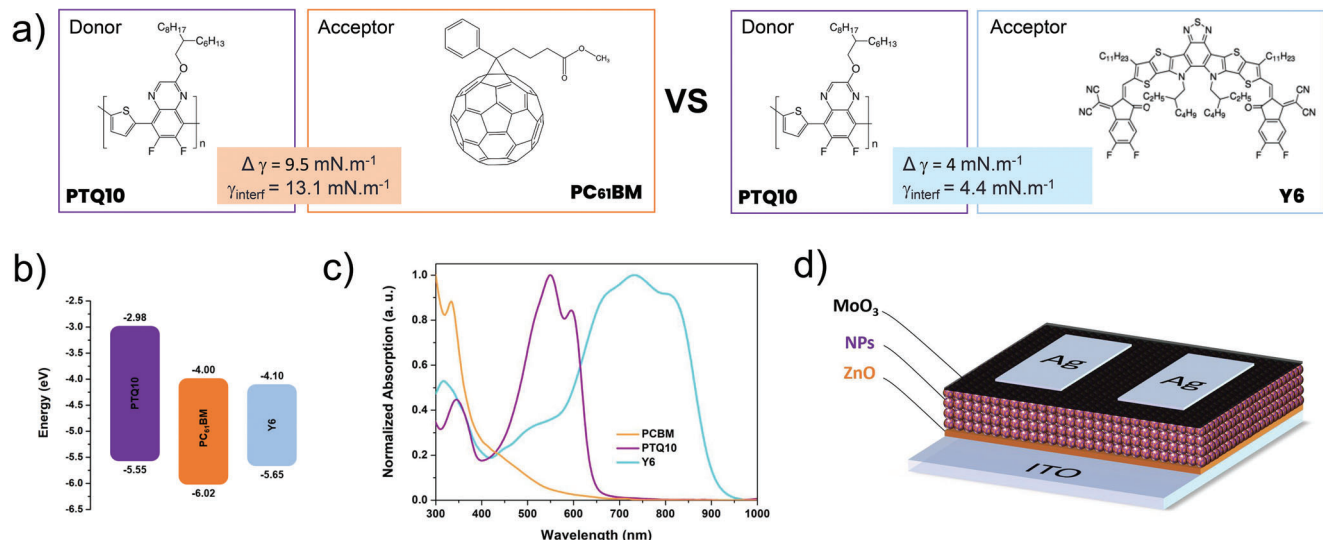


**Figure 1.** a) Chemical structures of the donor material (PTQ10) and the two acceptor materials (PC<sub>61</sub>BM, Y6) used in this study as well as surface energy differences and interfacial energies. b) Highest Occupied Molecular Orbital (HOMO) and Lowest Unoccupied Molecular Orbital (LUMO) of PTQ10, PC<sub>61</sub>BM, and Y6. c) Absorption spectra of PC<sub>61</sub>BM NP, PTQ10 NP, and Y6 NP (water-based dispersions). d) Schematic representation of organic photovoltaic devices fabricated from water-based colloidal dispersions.

pyrrolobenzothiadiazole) associated with a benzothiadiazole (BT) unit<sup>[33]</sup> (Figure 1). The PTQ10:PC<sub>61</sub>BM system shows high interfacial energy and surface energy difference while the PTQ10:Y6 system presents the opposite characteristics, with low interfacial energy and surface energy difference. With the combination of microscopy techniques [scanning transmission X-ray microscopy (STXM), transmission electron microscopy (TEM), atomic force microscopy (AFM)], we show that a large surface energy difference results in large phase separation within the NP as well as in the thin film after thermal annealing. As a result, low device efficiency is achieved, around 1% PCE for PTQ10:PC<sub>61</sub>BM based OPV devices, which is 60% lower than that of devices fabricated from organic solvent. On the other hand, PTQ10:Y6 NPs present initially an intermixed donor/acceptor morphology and large phase separation is not observed upon annealing. Consequently, a PCE of up to 9.98% is achieved, only 15% lower than the efficiency reached for devices fabricated from organic solvent. Thermal analysis [thermogravimetric analysis, differential scanning calorimetry (DSC)] highlighted the important role of the elimination of the surfactant as well as the melting of Y6 crystallites to enhance the sintering of the nanoparticles.

## 2. Results

### 2.1. Surface and Interfacial Energies

To investigate the influence of the surface energies on the morphology of nanoparticles and thin films and, as a consequence, on the photovoltaic properties, two donor/acceptor combinations were selected: PTQ10:Y6 and PTQ10:PC<sub>61</sub>BM. Surface energies ( $\gamma$ ), including dispersive ( $\gamma_D$ ) and polar ( $\gamma_P$ ) components, as well as the interfacial energy between the donor (PTQ10) and the acceptor (PC<sub>61</sub>BM or Y6) were determined from contact angles with water and ethylene glycol (EG) and using the method

described by Wu et al. (Table 1).<sup>[34]</sup> On the one hand, a large surface energy difference is calculated between PTQ10 and PC<sub>61</sub>BM (9.5 mN m<sup>-1</sup>) as well as a high interfacial energy of 13.1 mN m<sup>-1</sup> between the donor and the acceptor. On the other hand, when PTQ10 is associated with Y6 as acceptor, the surface energy difference is moderate (4 mN m<sup>-1</sup>) and the interfacial energy is much lower than that of PTQ10: PC<sub>61</sub>BM, around 4.4 mN m<sup>-1</sup>. Interfacial energy between the donor and the acceptor<sup>[35–37]</sup> as well as surface energy difference<sup>[31]</sup> has been shown to be an important factor driving the phase segregation in bulk heterojunction as well as in nanoparticles. A high interfacial energy generally leads to large phase separation while low interfacial energy enables intermixed morphology. Therefore, the influence of the difference in chemical compatibility between the donor (PTQ10) and the acceptors (PC<sub>61</sub>BM or Y6) on the nanomorphology of the particles is investigated in the following part.

### 2.2. NP Synthesis and OPV Devices Fabrication

Composite nanoparticles of PTQ10:Y6 and PTQ10:PC<sub>61</sub>BM have been synthesized using the mini-emulsion process (see the Experimental Section for complete description) using sodium dodecyl sulfate (SDS) as surfactant. The final dispersion ink was concentrated at 60 mg mL<sup>-1</sup> and the Z-average size of the nanoparticle was determined by dynamic light scattering (DLS) as 78 nm (Figure S1, Supporting Information). OPV devices were fabricated using the following inverted architecture: glass/ITO/ZnO/Active Layer/MoO<sub>3</sub>/Ag (Figure 1d) and current–voltage characterization was performed in the dark and under 1 sun illumination. The active layers (thickness,  $e = 115$  nm) are deposited either from water-based colloidal inks (np-BHJ) or organic solvent inks (BHJ). At first the influence of the thermal annealing on the np-BHJ has been studied for the two kinds of composite nanoparticles, PTQ10:PC<sub>61</sub>BM and

**Table 1.** Contact angles with water and ethylene glycol ( $^{\circ}$ ); dispersive, polar components and total surface energy ( $\text{mN m}^{-1}$ ) of PTQ10, PC<sub>61</sub>BM and Y6. Interfacial energy between PTQ10/PC<sub>61</sub>BM and PTQ10/Y6 ( $\text{mN m}^{-1}$ ).

Material	Solvent	Contact angle ( $^{\circ}$ )	$\gamma_D$ [ $\text{mN m}^{-1}$ ]	$\gamma_P$ [ $\text{mN m}^{-1}$ ]	$\gamma$ [ $\text{mN m}^{-1}$ ]	Interfacial energy ( $\gamma_{AB}$ ) with PTQ10 [ $\text{mN m}^{-1}$ ]
PTQ10	Water	104.8 $\pm$ 0.2	21.2	2.0	23.2	–
	EG	78.1 $\pm$ 0.4				
PC <sub>61</sub> BM	Water	78.1 $\pm$ 1.0	15.7	17.0	32.7	13.1
	EG	54.8 $\pm$ 0.4				
Y6	Water	91.5 $\pm$ 0.3	19.2	8.0	27.2	4.4
	EG	64.1 $\pm$ 0.2				

PTQ10:Y6 and compared with the control device made from organic solvent (BHJ). The photovoltaic characteristics of the different devices are summarized in **Table 2**.

### 2.2.1. PTQ10:PC<sub>61</sub>BM Water Processed OPV Devices

In the case of PTQ10:PC<sub>61</sub>BM based devices, one can clearly see that solar cells fabricated from water-based colloidal dispersions (np-BHJ) present much lower PCE compared to those fabricated from organic solvent (BHJ) (**Figure 2a**). In particular, short-circuit current density ( $J_{sc}$ ) is much lower, decreasing from 4.83 mA cm<sup>-2</sup> down to 2.51 mA cm<sup>-2</sup> as well as fill factor (FF), decreasing from 0.58 to 0.42. External quantum efficiency (EQE) confirms the lower efficiency of NP-based active layer in terms of photoconversion since only a maximum of 22% of incident photons generate electrons, twice lower than for the organic solvent based active layer (**Figure 2b**). Thermal annealing at 140, 170 or 200 °C of the active layer did not help to improve the performance of the solar cells, with PCE stuck around 1%.

### 2.2.2. PTQ10:Y6 Water Processed OPV Devices

On the other hand, OPV devices fabricated from water-based PTQ10:Y6 dispersions (PTQ10:Y6 np-BHJ) outperform the

fullerene-based counterparts (PTQ10:PC<sub>61</sub>BM np-BHJ). Even at low annealing temperatures (100 °C), devices present already 10.43 mA cm<sup>-2</sup> and 3.53% for  $J_{sc}$  and PCE respectively. Interestingly, with increasing annealing temperature and up to 200 °C, the performances of the devices continuously increases until it reaches an average of 8.08% as PCE, with  $J_{sc} = 18.13 \text{ mA cm}^{-2}$ , open-circuit voltage ( $V_{oc}$ ) = 714 mV and FF = 0.62 for 200 °C annealing temperature. The influence of the active layer thickness (Table S1 and Figure S2, Supporting Information) and the annealing conditions (Table S2, Supporting Information) was investigated. Optimal active layer thickness of 140 nm and annealing for 2 min at 200 °C is obtained, leading to PTQ10:Y6 organic solar cells prepared from water-based inks reached up to 9.60% PCE, with  $J_{sc} = 19.96 \text{ mA cm}^{-2}$ ,  $V_{oc} = 733 \text{ mV}$  and FF = 0.66. The influence of the NP size was also investigated (Table S3, Supporting Information). This result shows that by decreasing the size of the NP, higher  $J_{sc}$  are obtained resulting in a higher PCE. A record PCE was achieved for nanoparticles with average diameter of 55 nm, up to 9.98% ( $J_{sc} = 21.39 \text{ mA cm}^{-2}$ ,  $V_{oc} = 728 \text{ mV}$ , and FF = 0.64). This enhancement can be explained by an improved exciton dissociation thanks to smaller domain sizes. A similar effect was also observed by Xie et al.<sup>[38]</sup> In parallel, PTQ10:Y6 devices were fabricated from chloroform solution (PTQ10:Y6 BHJ) and characterized. Slightly higher performances were obtained with average PCE 11.2% ( $J_{sc} = 23.2 \text{ mA cm}^{-2}$ ,  $V_{oc} = 809 \text{ mV}$ , and FF = 0.60).

**Table 2.** Photovoltaic characteristics of OPV devices (active layer thickness = 115 nm) fabricated from water-based colloidal nanoparticle dispersions of PTQ10:PC<sub>61</sub>BM and PTQ10:Y6. Influence of the temperature of thermal annealing (5 min). Average values given for 8 individual devices.

	Solvent	TA [°C] (5 min)	$V_{oc}$ [mV]	$J_{sc}$ [ $\text{mA cm}^{-2}$ ]	FF	PCE (%)	
PTQ10:PC <sub>61</sub> BM (BHJ)	TMB	None	897 $\pm$ 11	4.83 $\pm$ 0.03	0.58 $\pm$ 0.01	2.52 $\pm$ 0.06	
PTQ10:PC <sub>61</sub> BM (np-BHJ)	Water	None	820 $\pm$ 10	2.51 $\pm$ 0.05	0.42 $\pm$ 0.01	0.86 $\pm$ 0.02	
		140	900 $\pm$ 10	2.54 $\pm$ 0.11	0.44 $\pm$ 0.01	1.01 $\pm$ 0.05	
		170	830 $\pm$ 20	2.43 $\pm$ 0.05	0.50 $\pm$ 0.01	0.93 $\pm$ 0.11	
		200	690 $\pm$ 10	2.65 $\pm$ 0.33	0.56 $\pm$ 0.01	1.02 $\pm$ 0.02	
PTQ10:Y6 (BHJ)	Chloroform	None	809 $\pm$ 5	23.15 $\pm$ 0.07	0.60 $\pm$ 0.02	11.19 $\pm$ 0.26	
PTQ10:Y6 (np-BHJ)		None	688 $\pm$ 13	7.97 $\pm$ 0.11	0.40 $\pm$ 0.02	2.22 $\pm$ 0.13	
		100	716 $\pm$ 17	10.43 $\pm$ 0.18	0.47 $\pm$ 0.02	3.53 $\pm$ 0.19	
		130	696 $\pm$ 33	12.61 $\pm$ 0.69	0.46 $\pm$ 0.04	4.04 $\pm$ 0.72	
		150	722 $\pm$ 10	14.65 $\pm$ 0.45	0.49 $\pm$ 0.03	5.22 $\pm$ 0.34	
		170	714 $\pm$ 13	16.90 $\pm$ 0.56	0.47 $\pm$ 0.03	5.64 $\pm$ 0.50	
		200	714 $\pm$ 15	18.13 $\pm$ 1.15	0.62 $\pm$ 0.01	8.08 $\pm$ 0.53	

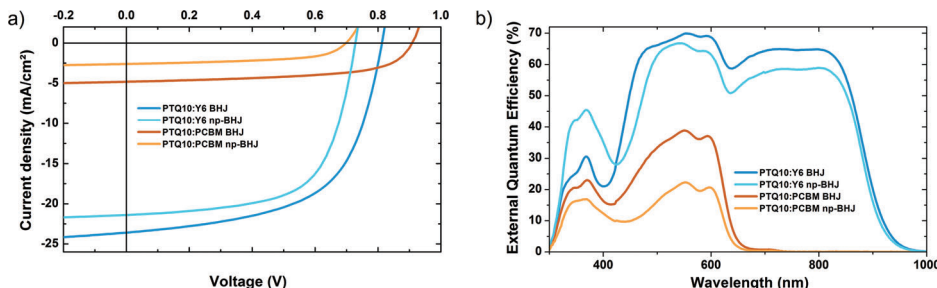


**Figure 2.** a) Current density–voltage ( $J$ – $V$ ) characteristics and b) external quantum efficiencies of PTQ10:Y6 np-BHJ (light blue, prepared from water based dispersions, NP diameter = 55 nm) thermally annealed at 200 °C for 2 min, PTQ10:Y6 BHJ (blue, prepared from organic solvent), PTQ10:PC<sub>61</sub>BM np-BHJ thermally annealed at 200 °C for 5 min (light orange, prepared from water based dispersions) and PTQ10:PC<sub>61</sub>BM BHJ (orange, prepared from organic solvent).

EQE spectra for both devices, water-based (np-BHJ) and organic solvent based (BHJ) are shown in Figure 2b, and one can observe that both devices present similar spectral shape, with contribution of both PTQ10, from 450 to 650 nm, and Y6, from 600 to 900 nm. For PTQ10:Y6 BHJ, up to 70% of incident photons generate electrons, with PTQ10 contributing to 70% and Y6 to 65%. On the other hand, for PTQ10:Y6 np-BHJ these values are a bit lower with a maximum EQE of 65% in the PTQ10 region but only 56% in the Y6 region.

Although lower than for organic solvent-based devices, these high EQE values suggest an adapted active layer morphology of PTQ10:Y6 np-BHJ. Devices prepared from organic solvent present also higher  $V_{oc}$  than those prepared from water-based colloidal inks, 0.82 and 0.73 V, respectively, but lower FF, 0.59 and 0.65, respectively. Although many factors can affect those characteristics, the change is attributed here to the nanoscale morphology. Indeed, it has been shown that higher degree of organization of the donor and/or the acceptor generally leads to lower  $V_{oc}$  due to energy level splitting<sup>[39,40]</sup> and higher FF due to better charge transport.<sup>[41]</sup> The key conclusion of the analysis of the photovoltaic performances is that PTQ10:Y6 np-BHJ present up to 85% of the PCE of PTQ10:Y6 device fabricated from organic solvent (BHJ) while PTQ10:PC<sub>61</sub>BM np-BHJ devices only achieved 40% of the PCE of its organic solvent-based counterpart.

Other surfactants were also tested, dodecylbenzene sulfonate (SDBS)<sup>[42]</sup> and the non-ionic surfactant Pluronic F127.<sup>[29]</sup> Using Pluronic F127, the macroemulsion and mini-emulsion was hardly achieved. The process of centrifugal dialysis led to the formation of aggregates which accumulated in the filter (Figure S3, Supporting Information). As a result, a concentrated colloidal ink was not possible to achieve with Pluronic F127 using the miniemulsion process. With SDBS, a concentrated colloidal ink was achieved with a concentration of 60 mg mL<sup>-1</sup> and OPV devices were fabricated using similar conditions to SDS-based inks. However much lower photovoltaic performances were achieved (Table S4, Supporting Information), with a maximum of 4.32% PCE for 170 °C. In particular,  $J_{sc}$  and FF are much lower than for SDS based dispersions and the thermal annealing at 200 °C, the optimum for SDS, leads to a total loss of performance. One can suggest that SDBS surfactant is more complicated to eliminate using centrifugal-dialysis and that the remaining amount is detrimental for the device performance. From this study on the influence of the surfactant, SDS seems to be the best choice and will be kept for the rest of the study.

### 2.3. Nanoparticle Morphological Investigation

In order to understand the reason behind such differences between PTQ10:PC<sub>61</sub>BM np-BHJ and PTQ10:Y6 np-BHJ, STXM and correlative transmission electron microscopy (TEM) were conducted on different NP assemblies: PTQ10:PC<sub>61</sub>BM unannealed and annealed at 200 °C (Figure 3) and PTQ10:Y6 unannealed and annealed at 170 or 200 °C (Figure 4). Focusing on the unannealed NP assemblies (Figure 3a–e and Figure 4a–e), one can observe a striking difference in the nanomorphology of the two kinds of nanoparticles. On the one hand, PTQ10:PC<sub>61</sub>BM NPs present a classical core–shell morphology, with donor-rich shell (Figure 3c) and acceptor-rich core (Figure 3d). On the other hand, PTQ10:Y6 NPs show an intermixed morphology. Indeed, no clear donor-acceptor phase-separation is observed within the nanoparticles (Figure 4c,d).

#### 2.3.1. PTQ10:PC<sub>61</sub>BM Nanoparticle Morphology

The type of core–shell morphology observed here for PTQ10:PC<sub>61</sub>BM NPs has been observed in several other donor:acceptor NP systems prepared by mini-emulsion, in particular for those prepared with fullerene derivatives.<sup>[21,23,25]</sup> It is attributed to the higher surface energy of the acceptor (fullerene derivatives) compared to the donor materials. Upon formation of the NP, the component with the lower surface energy tends to migrate to the solvent–water interface to minimize the free energy. While the shell is PTQ10-rich (75–90%), it is interesting to note that the composition of the core is more intermixed about 60% PC<sub>61</sub>BM/40% PTQ10 (Figure S4a, Supporting Information). In Table 1, one can observe that PC<sub>61</sub>BM has a much larger surface energy (32.7 mN m<sup>-1</sup>) than PTQ10 (23.2 mN m<sup>-1</sup>), similar to other kinds of donor/acceptor systems (P3HT, TQ1). This difference explains the nanomorphology of the PTQ10:PC<sub>61</sub>BM nanoparticles, with the outer shell predominantly composed of the lower surface energy element.<sup>[31]</sup>

Photoluminescence was performed on the nanoparticles dispersions to investigate the impact of such morphology on the exciton dissociation (Figure S5, Supporting Information). Even though core–shell, the quenching of the PTQ10 fluorescence is very effective up to 96%, indicating that exciton dissociation is highly efficient. Nevertheless, this morphology driven by the

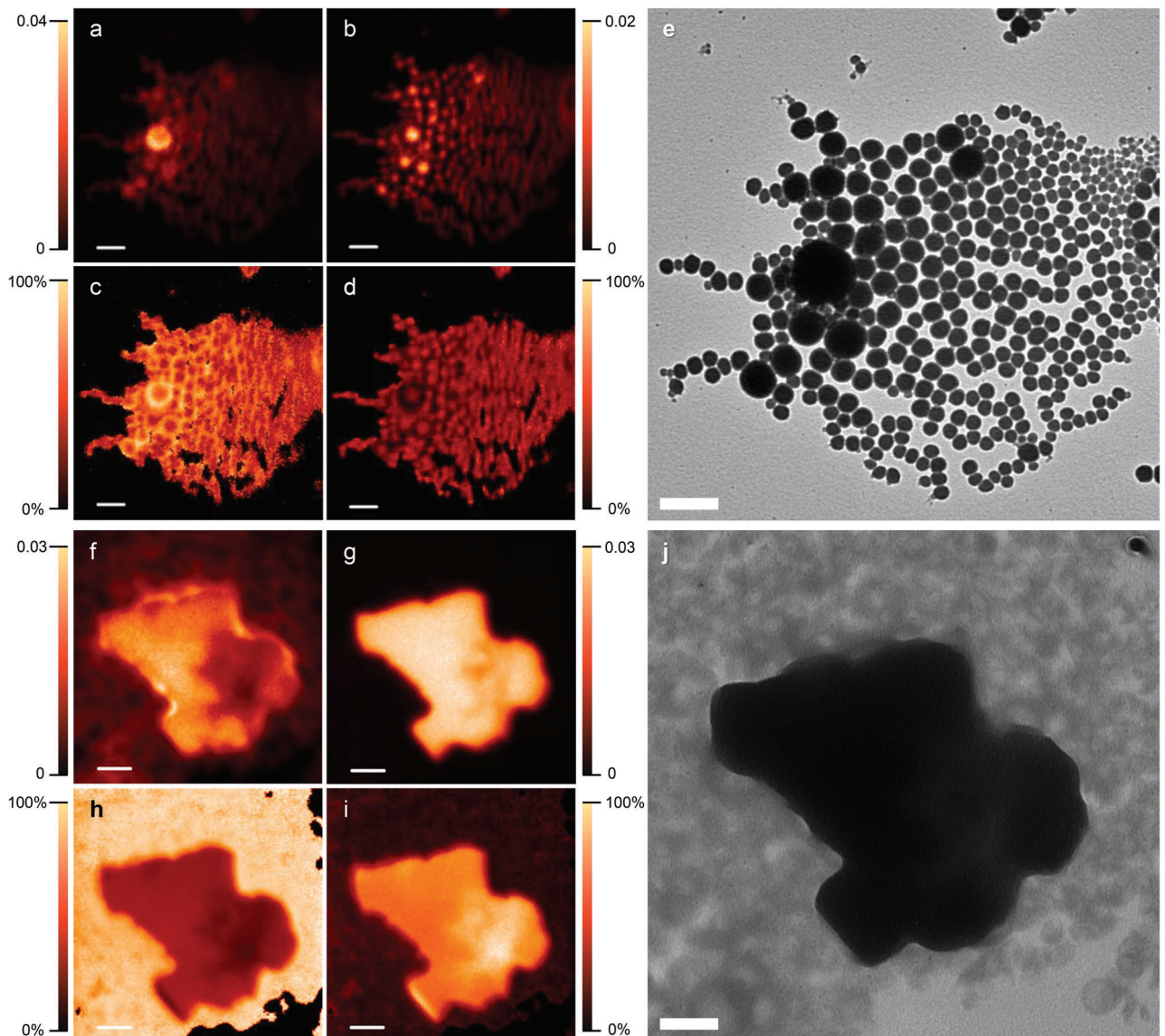


**Figure 3.** STXM composition maps of PTQ10:PC<sub>61</sub>BM NPs without thermal treatment: mass plots of a) PTQ10 and b) PC<sub>61</sub>BM, corresponding relative concentration of c) PTQ10 and d) PC<sub>61</sub>BM and e) position-matched TEM image. STXM composition maps of PTQ10:PC<sub>61</sub>BM NPs with 200 °C thermal treatment: mass plots of f) PTQ10 and g) PC<sub>61</sub>BM, corresponding relative concentration of h) PTQ10 and i) PC<sub>61</sub>BM and j) position-matched TEM image. All scale bars are 500 nm. The color contrast is scaled such that light colors correspond to higher component concentrations. For the mass plots (a,b,f,g) the color scale bars indicate concentration of component in milligrams per centimeter square.

surface energies seems not adapted to organic photovoltaic devices. The presence of an almost pure PTQ10 shell around the intermixed core can impede the electron transport. This could explain the low EQE value as well as the poor FF. As a result, PTQ10:PC<sub>61</sub>BM OPV devices with np-BHJ present only 40% of the performance of control OPV device prepared from organic solvent (BHJ).

### 2.3.2. PTQ10:Y6 Nanoparticle Morphology

Figure 4c,d shows the relative concentration of PTQ10 and Y6, respectively, in PTQ10:Y6 NPs before annealing. No clear phase

separation can be observed within the nanoparticles and the morphology seems to be intermixed. Radial composition profiles were extracted for several NPs and plotted in Figure S4b, Supporting Information. This analysis confirms that the initial morphology of PTQ10:Y6 is intermixed or with very small sub-domains below the resolution limit of STXM ( $\approx 30$  nm). This kind of morphology, often observed for NPs synthesized by nanoprecipitation, is rather uncommon for mini-emulsion based NPs. In general, the thermodynamic equilibrium leads to a core–shell morphology driven by the surface energy difference, even for non-fullerene acceptors.<sup>[31]</sup> In few cases intermixed morphology was identified as for PTB7-Th:eh-IDTBR NPs synthesized by the mini-emulsion process.<sup>[43]</sup> In their article, Kosco et al. man-

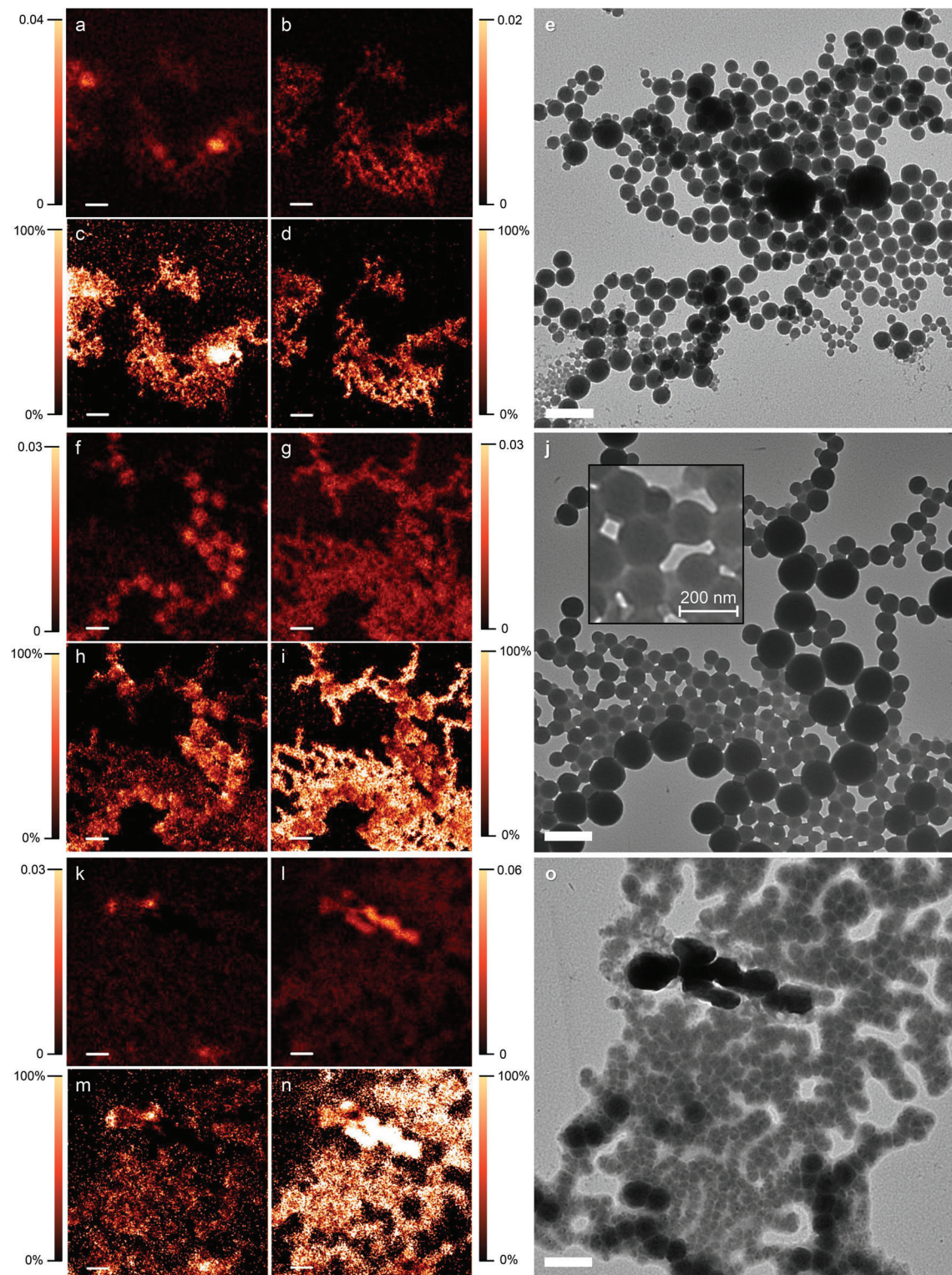


**Figure 4.** STXM composition maps of PTQ 10:Y6 NPs without thermal treatment: mass plots of a) PTQ10 and b) Y6, corresponding relative concentration of c) PTQ10 and d) Y6 and e) TEM image. STXM composition maps of PTQ10:Y6 NPs with 170 °C thermal treatment: mass plots of f) PTQ10 and g) Y6, corresponding relative concentration of h) PTQ10 and i) Y6 and j) position-matched TEM image. Inset: close-up look for better visualization of the sintering. STXM composition maps of PTQ10:Y6 NPs with 200 °C thermal treatment: mass plots of k) PTQ10 and l) Y6, corresponding relative concentration of m) PTQ10 and n) Y6 and o) position-matched TEM image. All scale bars are 500 nm. The color contrast is scaled such that light colors correspond to higher component concentrations. For the mass plots (a,b,f,g,k,l) the color scale bars indicate concentration of component in milligrams per centimeter square.

aged to tune the nanomorphology of the particle by changing the surfactant, equilibrating therefore the solvent–water surface tension for both materials. In the case of PTQ10:Y6, the surface energy difference between the donor and the acceptor is much lower than that of PTQ10:PC<sub>61</sub>BM, 4 and 9.5 mN m<sup>-1</sup>, respectively (Table 1). According to Barr et al.,<sup>[31]</sup> the lower the surface energy difference, the closer the nanomorphology is to an intermixed morphology which is a first explanation of the morphology observed for the PTQ10:Y6 system. In addition, the interfacial energy between PTQ10 and Y6 was also calculated as 4.4 mN m<sup>-1</sup>. Such a low value indicates that both materials have a low tendency to phase segregate (demix) confirming that the morphology should be closer to intermixed.<sup>[44]</sup> Photoluminescence of PTQ10:Y6 nanoparticles was also performed (Figure S5, Supporting Information). While PTQ10 fluorescence (650–950 nm) is totally quenched, one can clearly still see that of the Y6 (800–1150 nm) is only quenched by 85%. This result allows to refine the morphology, which seems not to be molecularly intermixed but with distributed nanodomains of pure Y6.

### 2.3.3. Impact of Thermal Treatment on Thin Films (NP Assemblies) Morphology

Focusing now on the impact of thermal annealing on the NP assemblies PTQ10:PC<sub>61</sub>BM and PTQ10:Y6, one can observe that the evolutions are drastically different. On the one hand, thermal annealing at 200 °C has a dramatic effect on the phase separation between PTQ10 and PC<sub>61</sub>BM. Figure 3h,i shows large clusters (2–4 μm) composed mostly of PC<sub>61</sub>BM (≈62%) surrounded by PTQ10 highly rich areas (89%). This tendency to phase segregate is the result of the high interfacial energy between the donor and the acceptor, 13.1 mN m<sup>-1</sup>, enhancing the phase segregation between the donor and the acceptor. From the TEM image (Figure 3j), one can notice that the NP shape has disappeared, indicating that the NPs have merged in the form of a thin film (sintering). As expected, this evolution of the active layer morphology with large scale separated domains did not lead to an improvement of the OPV performance. Thermal annealing at 140, 170 or 200 °C of PTQ10:PC<sub>61</sub>BM np-BHJ resulted in devices with 1.01%, 0.93% and 1.02% PCE, respectively. The fill factor seems to be improved with increasing thermal annealing temperature as a result of the sintering of the nanoparticles, but, concomitantly V<sub>oc</sub> decreases as a result of the formation of large phase-separated domains.<sup>[40]</sup>

Thermal annealing has a totally different effect on PTQ10:Y6 np-BHJ. STXM images of NP assemblies annealed at 170 (Figure 4f–i) and 200 °C (Figure 4k–n), did not show large phase separation of donor and acceptor materials. With a thermal annealing treatment at 170 °C, it is still possible to detect the intermixed morphology within a single composite nanoparticle, with randomly distributed donor-rich and acceptor-rich domains clearly observed on the radial composition profiles (Figure S4c, Supporting Information). With a thermal annealing treatment at 200 °C, radial composition profiles of individual nanoparticles were not possible since they do not show clear borders due to sintering. Instead, a composition profile in a representative area was extracted, which still shows an intermixed morphology (Figure S6, Supporting Information), similar to the unannealed

nanoparticles and those annealed at 170 °C. Interfacial energy between PTQ10 and Y6 is only 4.4 mN m<sup>-1</sup> and such a low value can explain the stability of the nanoscale morphology and the absence of large phase separation upon thermal treatment. TEM images taken for unannealed samples (RT) and samples annealed at 100, 140, 170 and 200 °C, reveal that high temperatures are necessary to merge the nanoparticles. At room temperature, nanoparticles are well separated and the boundaries between two particles are still visible (Figure 4e). At low annealing temperatures of 100 and 140 °C (Figure S7a,b, Supporting Information), the particle shape is still clearly visible but coalescence of the nanoparticles starts: the boundaries between them are not as clear as for unannealed NPs. At 170 °C, the coalescence process is more pronounced as the boundaries between the particles are fading away, but the shape of the NPs is still clearly observable (Figure 4j). Finally, at 200 °C, the coalescence of the particles is fully effective (Figure 4o). Although, it is still possible to identify the original nanoparticle shape, they have all merged into a homogeneous thin film. AFM images before and after annealing were also taken (Figure S8, Supporting Information) and one can observe that surface roughness ( $R_{\text{rms}}$ ) decreases from 7.95 to 5.64 nm upon annealing, confirming the coalescence of the particles. The evolution of the photovoltaic performance reflects that of the morphology detected by STXM and TEM. Indeed, the thermal annealing leads to the coalescence of the NPs, essential for efficient charge transport. Such phenomenon starts at 170 °C but it is highly effective at 200 °C. Furthermore, creation of conduction pathways is also confirmed with EQE measurements (Figure S9, Supporting Information). Although the initial intimate morphology (PTQ10:Y6 np-BHJ, no annealing) results in efficient exciton dissociation (Figure S5, Supporting Information), only 33% of incident photons generate electrons which illustrates the lack of conduction pathways for the charges. On the other hand, EQE increases up to 65% with samples annealed at 200 °C. As a result, the FF is improved with increasing annealing temperatures, up to 0.66 for optimized thermal treatment (Table S2, Supporting Information, 200 °C, 2 and 5 min). Concomitantly, the nanoscale morphology is not affected even at high annealing temperature and nano-domains of donor and acceptor materials with size approaching the resolution of STXM (≈30 nm) are still detected within a single NP. The combination of these two phenomena explains the high performance achieved with a record average PCE of 9.55% for PTQ10:Y6 np-BHJ annealed at 200 °C for 2 min (Table S3, Supporting Information).

### 2.4. Correlation with Physico-Chemical Analysis

A transition after 170 °C is clearly observed on the photovoltaic performances of PTQ10:Y6 np-BHJ, with PCE going from 4–6% (for 130, 150, and 170 °C) to more than 8% (for 200 °C). Especially, short-circuit current density increases up to 20–22 mA cm<sup>-2</sup> and FF rises above 0.60. STXM and TEM analysis suggest that morphology is modified at this temperature, especially with the sintering of the nanoparticles. In order to go deeper in the understanding, thermogravimetric analysis (TGA) and DSC were performed on pure materials (PTQ10, Y6, and SDS) as well as on PTQ10:Y6 NPs, under nitrogen atmosphere, and the resulting thermograms are presented in Figure 5.

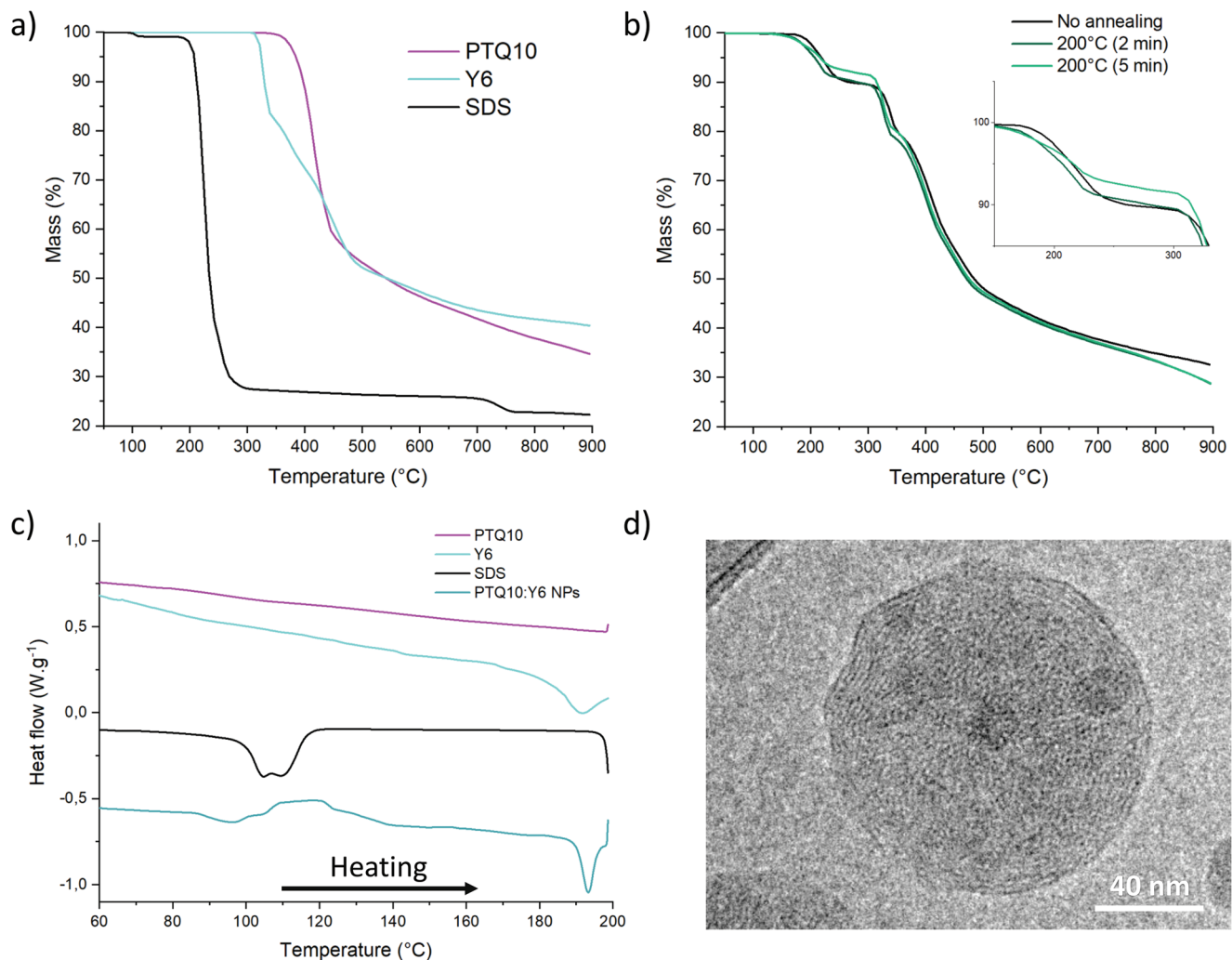


**Figure 5.** a) Thermogravimetric analysis on SDS, PTQ10 and Y6 and b) as well as on PTQ10:Y6 NPs with different thermal treatment: no annealing, 2 min at 200 °C and 5 min at 200 °C. Onset in panel (b) highlights the degradation of SDS between 150 and 330 °C. Differential scanning calorimetry c) heating thermograms for PTQ10, Y6, SDS, and PTQ10:Y6 NPs. d) Cryo-TEM images of unannealed PTQ10:Y6 nanoparticles showing crystallines domains of Y6.

TGA was performed on pure materials SDS, Y6, and PTQ10 (Figure 5a) and on PTQ10:Y6 NPs with different annealing conditions: no annealing, 2 min at 200 °C and 5 min at 200 °C (Figure 5b). Focusing on single materials, one can observe that the main degradation of the two organic semiconductors happens at high temperatures, 350–450 °C for PTQ10 and between 300–475 °C for Y6. On the other hand, SDS degradation begins much sooner, between 180 and 300 °C. TGA was also performed on PTQ10:Y6 NPs, with and without annealing in order to detect and estimate the remaining SDS content. For unannealed materials, the proportion of SDS (weight%) with respect to the overall mass is estimated at 15% according to TGA. This SDS value is expected to be the minimal SDS amount required for stabilization of the nanoparticles since five washing steps were performed. Interestingly, when the nanoparticles are exposed to a thermal annealing treatment at 200 °C prior to TGA (see procedure in the Experimental Section), this proportion decreases down to 14% and 11% for 2 and 5 min at 200 °C, respectively. Therefore, the

thermal annealing at 200 °C seems to favor the elimination of SDS surfactant through a degradation process.

The DSC thermogram of PTQ10 did not show any features during heating (Figure 5c) and cooling ramps (Figure S10, Supporting Information) in the range of temperature measured in accordance with previous literature,<sup>[32,45]</sup> indicating that no measurable phase transition happens up to 200 °C. Neat Y6 is clearly different and present an endothermic peak at 192 °C on the heating trace (Figure 5c) and exothermic one at 183 °C on the cooling traces (Figure S10, Supporting Information). They correspond respectively to the melting and recrystallization of Y6 crystals.<sup>[33,46]</sup> The heating thermogram of SDS reveals that the surfactant shows a broad endothermic peak centered around 105 °C, attributed to the fusion of SDS crystals (Figure 5c). PTQ10:Y6 NPs first heating thermogram present three peaks: an endothermic peak centered at 96 °C which corresponds to the fusion of SDS crystals, quickly followed by an exothermic broad peak centered at 120 °C. The origin of this second peak can be

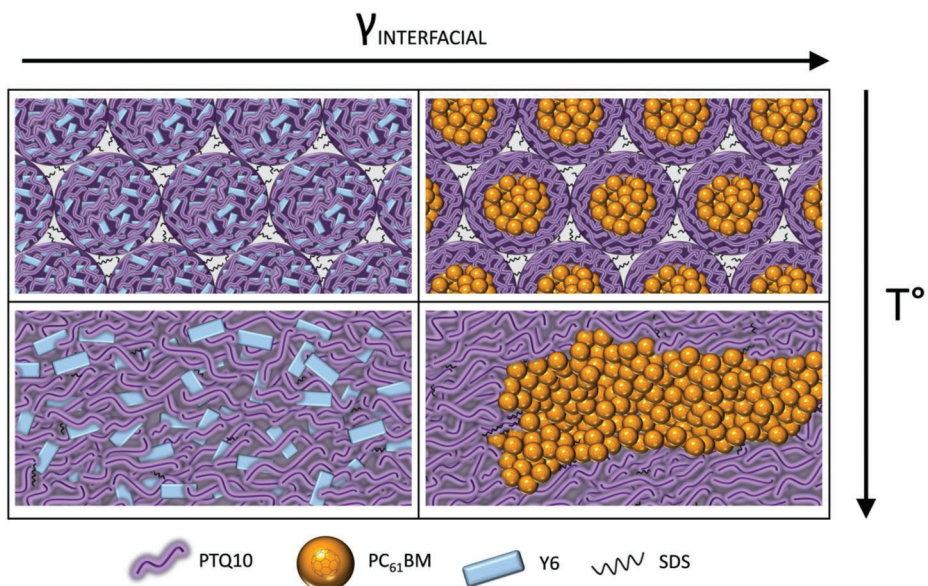


**Figure 6.** Schematic diagram of morphological changes in PTQ10:Y6 (left) and PTQ10:PC<sub>61</sub>BM (right) films upon thermal annealing.

related to Y6 cold crystallization,<sup>[47]</sup> probably helped by the mobility gained from SDS melting. The cold crystallization means that the mini-emulsion process and the interaction with PTQ10 or SDS do not allow complete crystallization of the acceptor. This also reveals that the crystalline volume of Y6 in the nanoparticles can be increased by thermal annealing. Finally, a third endothermic peak is measured at 193 °C, corresponding to the fusion of Y6 crystalline domains. This temperature correlates precisely with the sharp increase of OPV performance (Table 1) and the sintering of the PTQ10:Y6 nanoparticles observed with TEM analysis (Figure 4o).

Cryo-TEM images were taken on water dispersed PTQ10:Y6 NPs to confirm the presence of crystalline domains within the composite nanoparticles prepared by mini-emulsion (Figure 5d, and additional images in Figure S11, Supporting Information). Images clearly show lamellar arrangements in different areas for a single nanoparticle, confirming therefore its poly-crystalline nature.

These results lead us to propose the following tentative mechanism (**Figure 6**).

PTQ10:PC<sub>61</sub>BM nanoparticles present initially a core–shell morphology due to high surface energy difference between the donor and the acceptor. Upon annealing, large phase separation occurs due to high interfacial energies. As a result, PTQ10:PC<sub>61</sub>BM nanoparticle-based devices present low efficiency compared to those prepared from organic solvent ( $\approx 40\%$ ).

On the contrary, PTQ10:Y6 nanoparticles prepared by mini-emulsion present an intermixed donor/acceptor morphology with Y6 crystalline nanodomains. In order to achieve its full PV efficiency, interconnection of the domains, and thus the nanoparticles, is required. This is achieved by thermal annealing of 200 °C, a temperature at which the SDS starts to degrade and fusion of the Y6 crystallites occurs. Due to a low interfacial energy between the donor (PTQ10) and the acceptor (Y6), the thermal annealing did not lead to large phase separation. As a result, only the sintering of the nanoparticles occurs, and high OPV effi-

ciency is reached, around 85% of that achieved with devices fabricated from organic solvent.

## 2.5. Stability

Lifetime of organic photovoltaic devices is an important aspect to assess. A preliminary investigation has been conducted in order to understand the possible impact of the remaining surfactant on the stability of the OPV devices. Control and water-processed devices were fabricated from organic solution (PTQ10:Y6 BHJ) and water-based colloidal dispersion (PTQ10:Y6 np-BHJ), respectively. The devices were submitted for up to 530 h to continuous illumination (AM 1.5G, 1000 W m<sup>-2</sup>, open-circuit condition, with UV filter) to simulate ageing in real-life conditions. The evolutions of the different photovoltaic parameters are plotted in **Figure 7**.

A burn-in is observed in the first 20 h for both types of devices and leads to  $\approx 15\%$  loss of efficiency. After this period, the PCE stabilizes at around 8% and a slower degradation takes place. No significant differences are observed between PTQ10:Y6 BHJ and PTQ10:Y6 np-BHJ, both types of devices presenting the same stability. This important result highlights that the remaining surfactant is not detrimental for the device stability under these ageing conditions. Interestingly, the FF of devices fabricated from water-based dispersion seems to be more stable than the control device. A tentative explanation could be that the presence of surfactant stabilizes the active layer morphology. Additional experiments are ongoing to confirm and understand this stabilization phenomenon. Nevertheless, this study highlights that efficient OPV devices, up to 9.98% PCE, can be fabricated from water-based dispersions with stability comparable to control devices fabricated from organic solvent.

More generally, this study opens the route for the development of environmentally friendly processes for highly efficient organic photovoltaic devices and modules. Indeed, the development of

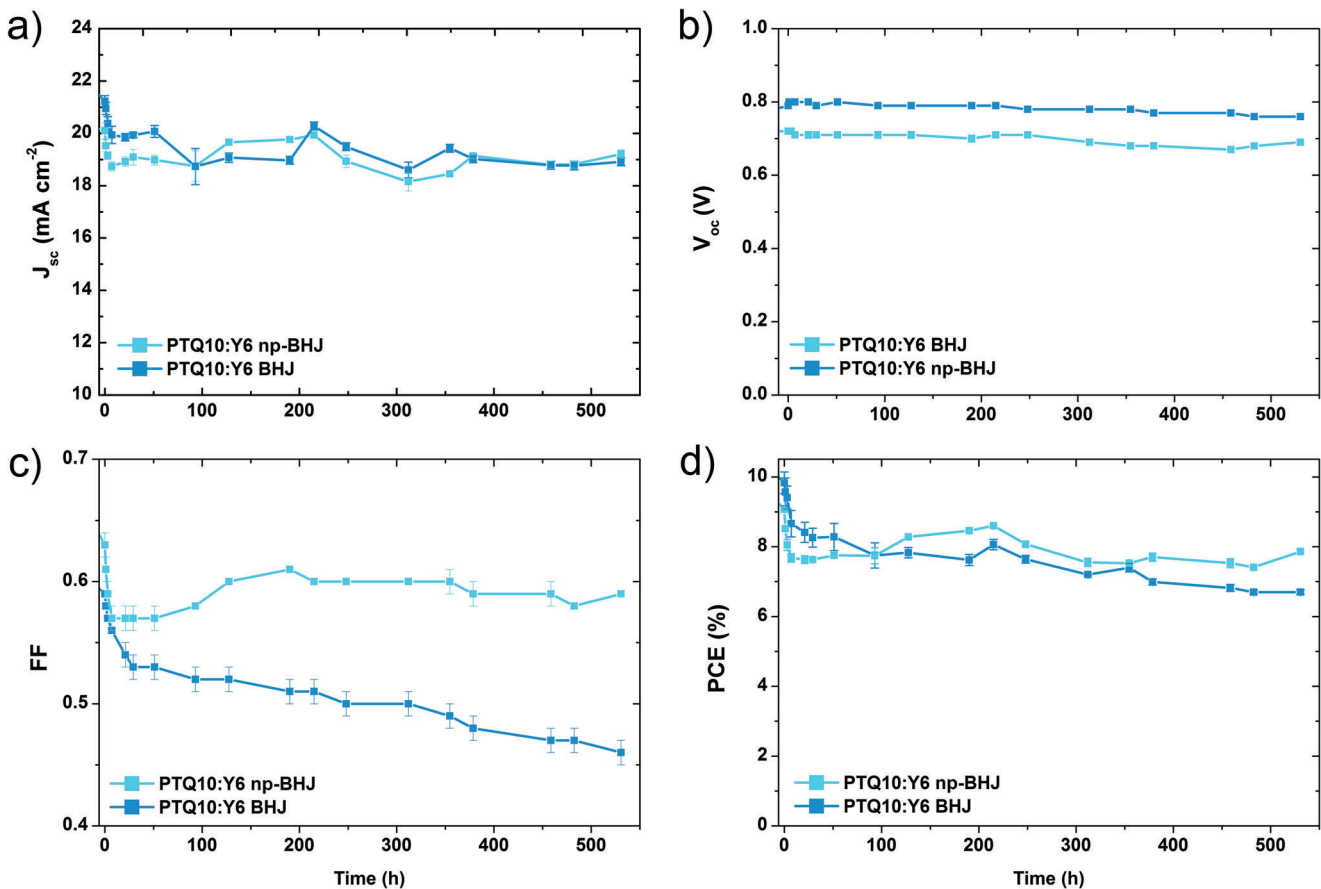


**Figure 7.** Evolution of the photovoltaic performances of OPV devices prepared from organic solvent inks (deep blue) and water-based colloidal inks (light blue): a)  $J_{sc}$ , b)  $V_{oc}$ , c) FF, and d) PCE.

non-fullerene acceptors allowed the OPV community to access a library of acceptor materials with specific physico-chemical properties, in particular with lower surface energies compared to the commonly used fullerene derivatives. This development opened the route for designing nanoparticles with specific morphologies (donor-rich core/acceptor-rich shell and acceptor-rich core/donor-rich shell)<sup>[31,48]</sup> or in this case intermixed morphology. This strategy of morphology control has been shown to be efficient for polymer/NFA as well as for all-polymer systems.<sup>[31]</sup> Further research is currently underway to evaluate the universality of this strategy in terms of device performance.

### 3. Conclusions

Efficient organic solar cells with PCE up to 9.98% were fabricated from water-based organic semiconductor colloidal dispersions prepared by mini-emulsion. The choice of the donor/acceptor is critical to achieving high performance organic solar cells made from water-based dispersions. Indeed, the low surface energy difference as well as low interfacial energy, available for PTQ10:Y6, allows for the fabrication of donor/acceptor nanoparticles with low phase segregation and intermixed morphology. In addition, the internal morphology of the nanoparticle was not dramatically changed upon thermal annealing, contrary to donor/acceptor nanoparticles that have a high surface energy difference such

as PTQ10:PC<sub>61</sub>BM. Although the internal morphology of the PTQ10:Y6 nanoparticles is suited for organic photovoltaics, thermal annealing up to 200 °C is necessary to achieve high performance. At this temperature, nanoparticles sintering occur. This correlates with the temperature of fusion of Y6 crystalline nanodomains present in the nanoparticles as well as the beginning of SDS degradation. The combination of these three phenomena: i) stable donor/acceptor intermixed morphology, ii) fusion of Y6 crystallites and nanoparticle sintering, and iii) degradation/elimination of SDS results in OPV devices that achieve a PCE that is 85% of the PCE of PTQ10:Y6 devices prepared with organic solvents. From our knowledge, 9.98% PCE is the highest performance achieved for water processed OPV devices without additives.

### 4. Experimental Section

**Materials:** Chloroform ( $\geq 99\%$ ), 1,2,4-trimethylbenzene TMB ( $\geq 98\%$ ), ethanolamine ( $\geq 99.5\%$ ), ethanol ( $\geq 99.8\%$ ), zinc acetate dihydrate, SDS, sodium dodecylbenzenesulfonate (SDBS), and Pluronic F127 were purchased from Sigma Aldrich. MoO<sub>3</sub> powder was purchased from NEYCO. Deionized water was obtained from a PURELAB Flex system ( $\approx 15 \text{ M}\Omega$ ). PTQ10 ( $M_w = 60 \text{ kDa}$ ) and Y6 were purchased from Brilliant Matters. PC<sub>61</sub>BM was purchased from Solaris Chem Inc. All the materials were used as received without further purification.

**Nanoparticles Synthesis:** Water-based inks were obtained with mini-emulsion synthesis. For the organic phase, 25 mg mL<sup>-1</sup> of donor/acceptor (wt% of 1:1.2) mixture was first dissolved in chloroform stirred for 2 h at 65 °C in a nitrogen-filled glovebox. Aqueous phase was obtained by dissolving 5 mg mL<sup>-1</sup> of surfactant (SDS, SDBS, or Pluronic F127) in deionized water and stirred for 30 min at RT.

A macroemulsion was then obtained by adding the organic phase into the aqueous phase (1:5 volume ratio) and stirred for 1 h at 40 °C (1000 rpm). The mini-emulsion dispersion was formed by sonicating the macro-emulsion using a BRANSON Digital Sonifier 450 in an ice-water bath for 2 min at 17% of the maximum power. Chloroform evaporation was done by stirring the mini-emulsion 3 h at 65 °C. Finally, in order to eliminate the excess of surfactant and concentrate the inks at 60 mg mL<sup>-1</sup>, centrifugal step was carried out by using Amicon Ultra-15 centrifuge filter (cut-off 100 kDa) and Hettich Universal 320 centrifugal. Five centrifugation cycles were done at 2200 rpm for 9 min. The retentate was raised to 15 mL with deionized water between each step.

For STXM experiments, the nanoparticles synthesis was modified in order to obtain large nanoparticles for better observation of the nanoparticle morphology. For the organic phase, 30 mg mL<sup>-1</sup> of donor/acceptor (wt% of 1:1.2) mixture was first dissolved in chloroform stirred for 2 h at 65 °C in a nitrogen-filled glovebox. Aqueous phase was obtained by preparing 0.18 mg mL<sup>-1</sup> of SDS in deionized water and stirred for 30 min at RT. The organic phase was injected in the aqueous phase (ratio 1:2.5) and then stirred at 1000 rpm at room temperature for 1 h to obtain the macro-emulsion. The mini-emulsion was obtained by sonicating the macro-emulsion with a GoldenWall 300 W sonicator (50%, 2 min). Chloroform was evaporated by stirring the mini-emulsion for 3 h at 65 °C. Finally, in order to eliminate the excess SDS, dialysis was performed using Slide-a-Lyzer dialysis cassette (cut-off 100 kDa). To synthesize different NP sizes, initial concentration of OSC in the organic phase had been varied. 35 and 15 mg mL<sup>-1</sup> of PTQ10:Y6 mixture was dissolved in chloroform to obtain 55 and 80 nm, respectively. The volume of the aqueous phase and the organic phase were adapted in order to keep the same amount of OSC weight in the mini-emulsion before the centrifugal step. SDS concentration in the aqueous phase remained the same as the parameters used for the macro and mini-emulsion steps.

**Dynamic Light Scattering:** Hydrodynamic diameters of the nanoparticles were determined by dynamic light scattering using a Zetasizer Nano ZS from Malvern Instruments at a detection angle of 173°. Autocorrelation curves were averaged from 10 to 15 acquisitions depending on the intensity of the scattered signal. The cumulants method was used to determine the Z-average hydrodynamic diameter and the polydispersity index width (PDI width). Three measurements were performed for each sample.

**Devices Fabrication:** OPV devices were fabricated with an inverted architecture glass/ITO/ZnO/active layer/MoO<sub>3</sub>/Ag, where ZnO and MoO<sub>3</sub> were used as electron transport (ETL) and hole transport (HTL) interlayer, respectively. The ITO covered glasses (1.5 × 1.5 cm<sup>2</sup>, 10 Ω□, VisionTek) were cleaned by sequential ultrasonic treatments: diluted soap Hellmanex III, deionized water and isopropanol. The ZnO precursor solution was prepared by mixing zinc acetate dihydrate (165 mg) and ethanolamine (90 µL) with ultrapure ethanol (5 mL). The solution was then stirred at 55 °C in air for 30 min and left at room temperature under continuous stirring prior to deposition. Before depositing the ETL, the substrates were dried and treated by UV-ozone for 15 min. ZnO precursor solution was then spin-coated to form 40 nm thin films. The substrates were then thermal annealed in air at 180 °C for 30 min. For np-BHJ active layers, substrates were treated by UV-ozone for 20 min before deposition in order to increase the hydrophilicity of the surface. np-BHJ active layers were obtained by spin coating on ZnO-covered substrates the nanoparticle dispersions with a rotation speed of 3000 rpm (for 140 nm). For BHJ active layers obtained from organic solvents, OSC solutions were prepared by dissolving 16 mg mL<sup>-1</sup> of PTQ10:Y6 (wt% of 1:1.2) mixture in chloroform stirred for 2 h at 65 °C in a nitrogen-filled glovebox. And for PTQ10:PC<sub>61</sub>BM (wt% of 1:1.2), 24 mg mL<sup>-1</sup> were dissolved in TMB stirred for 2 h at 70 °C in a nitrogen-filled glovebox. Both solutions were spin coated with a rotation speed of 1000 rpm. Afterward, vacuum evaporation ( $P = 10^{-6}$  mbar) was

used to deposit HTL MoO<sub>3</sub> (7 nm thick with a rate of 0.5 Å s<sup>-1</sup>) and electrode Ag (80 nm thick with a rate of 2 Å s<sup>-1</sup>). The area of OPV devices was 10.5 mm<sup>2</sup>.

**Current-Voltage Characterization:** A solar simulator using a xenon source and AM 1.5 G filters (Newport LCS-100) was used. The light intensity of the lamp was set at 100 mW cm<sup>-2</sup> using a calibrated silicon reference cell from Newport Co. The J-V curves were recorded in the dark and under 1-sun using a Keithley 2400 SMU, and parameters were directly extracted via a LabVIEW program. J-V characterization was done in a nitrogen-filled glovebox. Stability test was performed under continuous light illumination (Xenon source, UV filter with cut-off at 400 nm, 100 mW cm<sup>-2</sup>) and under open-circuit voltage conditions. The devices were tested regularly.

**External Quantum Efficiency:** EQE measurements were carried out using a PVE300 Photovoltaic EQE from Bentham Co. EQE was performed in ambient atmosphere and all OPV devices were encapsulated. J-V curves were re-recorded afterward to verify the good encapsulation.

**NEXAFS, STXM, and Correlative TEM:** NEXAFS at the C K-edge was utilized for the measurement of organic semiconductors in this study. Measurements of nanoparticle dispersions, PTQ10, Y6 and PC<sub>61</sub>BM were performed at two synchrotron beamlines, the PolLux<sup>[49,50]</sup> beamline (X07DA) at the Swiss Light Source (SLS) (Villigen, Switzerland) and the Polymer STXM 5.3.2.2 beamline of the Advanced Light Source (ALS) (Berkeley, USA). Second- and third-order light was removed, at the SLS, by an order sorting aperture and higher order suppressor (further details are provided in Frommherz et al.),<sup>[51]</sup> and at the ALS by an order sorting aperture and an N<sub>2</sub> gas filter (further details are provided in Kilcoyne et al.).<sup>[52]</sup> The transmitted X-ray beam was detected by a scintillator and a photomultiplier tube. The STXM Fresnel zone plate (Ni at SLS, Au at ALS) had an outermost zone width of 25 nm, setting the spatial resolution limit of the measurement.

Pristine films of each organic semiconductor material were prepared by spin coating chloroform or chlorobenzene solutions of each material onto PEDOT:PSS (Clevios PH from Heraeus) coated glass substrates. 2 × 2 mm<sup>2</sup> sections were scored on the films using a scalpel, followed by floating off the film sections onto a D.I. water surface, which was made possible by dissolving the PEDOT:PSS sacrificial layer under the semiconductor material films (for floating off method refer to He et al.).<sup>[51]</sup> 2 × 2 mm<sup>2</sup> film sections were subsequently collected onto 300 mesh Cu grids (20 µm bar, 63 µm hole and 3 mm diameter, purchased from ProSciTech Pty. Ltd.) for NEXAFS measurements. Nanoparticle dispersion sample were prepared for STXM measurements by spin coating 2.5 µL of dispersions onto low stress silicon nitride (Si<sub>3</sub>N<sub>4</sub>) membrane windows (window dimensions 1 × 1 mm<sup>2</sup>, window thickness 30 nm, silicon frame dimensions 5 × 5 mm<sup>2</sup>, purchased from Silson, UK) at 3000 rpm, 1 min, low acceleration. Samples were air dried at room temperature. NEXAFS linescans were performed for each pristine material film, and the energy of the X-ray beam was varied between 278 and 390 eV, spanning the C K-edge region. Orthogonal energies for later STXM mapping were selected by overlaying NEXAFS spectra of each donor:acceptor material combination, PTQ10:Y6 and PTQ10:PC<sub>61</sub>BM. Nanoparticle samples on Si<sub>3</sub>N<sub>4</sub> windows were loaded in the STXM sample chamber and rastered with respect to the X-ray beam. Singular value decomposition (SVD) was used to fit a sum of the pristine material NEXAFS spectra to the measured blend spectrum of the nanoparticles, at each pixel in the STXM images. Prior to singular value decomposition (SVD) fitting, the pristine material NEXAFS spectra were normalized to film thickness. The method of reference spectrum normalization involves dividing the real spectrum by a theoretical spectrum calculated based on the material's chemical formula using henke.lbl.gov/optical\_constants/filter, in order to convert the absorbance spectrum into the mass absorption coefficient. The aXis2000 package (unicorn.mcmaster.ca/aXis2000.html) was used to perform image analysis of STXM maps. Further details of STXM experimental methods and data analysis methods can be found in the literature.<sup>[53]</sup> Correlative TEM was used post-STXM to reimaging the same nanoparticles for collecting position-matched micrographs. The Si<sub>3</sub>N<sub>4</sub> membrane substrates with deposited nanoparticles were transported back to the University of Sydney (Australia) to measure TEM on a JEOL JEM-1400 at an

accelerating voltage of 120 kV, using a Norcada custom TEM holder for  $\text{Si}_3\text{N}_4$  membrane substrates (NTS-J-NX5-001).

**Cryo-TEM:** The principle of Cryo-TEM of vitrified specimens was previously described by Dubochet et al. in 1988.<sup>[54]</sup> The vitrification of the samples was carried out in a homemade vitrification system. The chamber was maintained at 22 °C, and the relative humidity was 80%. A 5  $\mu\text{l}$  drop of the sample was deposited onto a lacey carbon film covered with a 300 mesh Cu grid (Ted Pella-USA) rendered hydrophilic using an ELMO glow discharge unit (Cordouan Technologies, Pessac, France). The grid was automatically blotted to form a thin film and plunged in liquid ethane at -190 °C, as maintained by liquid nitrogen. Thus, a vitrified film was obtained in which the native structure of the vesicles was preserved. The grid was mounted onto a cryo holder (Gatan 626-Pleasanton, CA, USA) and observed under low-dose conditions ( $10 \text{ e}/\text{A}^2$ ) in a Tecnai G2 microscope (FEI, Eindhoven, Netherlands) at 200 kV. Images were acquired using an Eagle slow scan CCD camera (FEI).

**Thermal Gravimetric Analysis:** TGA was performed on a TGA 2, Mettler Toledo STAR system with a heating rate of 10 °C min<sup>-1</sup> under nitrogen atmosphere. For the PTQ10:Y6 nanoparticle dispersions, they were first freeze-dried using a CRIOS-80, Cryotec in order to remove the aqueous dispersant. The nanoparticles were then recovered in an alumina crucible and characterized in TGA. For the sample annealed prior to any characterization, annealing was performed directly inside of the crucible in glove box for 2 and 5 min.

**Differential Scanning Calorimetry:** DSC measurements were performed on a DSC 3, Mettler Toledo STAR system under a nitrogen atmosphere. For each sample, the temperature was increased from 25 to 200 °C at 10 °C min<sup>-1</sup>, then cooled down to 25 °C following the same ramp. This process was repeated for a second cycle. For PTQ10:Y6 NPs, only one cycle was performed, representative of the processing conditions used during device preparation.

**Contact Angle:** The surface energies of the different surfaces were determined using a Krüss DSA 100 goniometer by the method proposed by Wu et al.<sup>[34]</sup> based on the contact angle measurements of two different liquids on the substrate surface at 20 °C in static mode. The results correspond to the mean of at least 3 measurements.

**Atomic Force Microscopy:** A Bruker Innova AFM was used in tapping mode to record the height and phase images. Oxford Instruments cantilevers with 160 microns lengths were used (AC-160-TS) were used at their resonant frequency ( $\approx 300 \text{ kHz}$ ). Scan speed was set between 0.7 and 1 Hz and 512 lines/image resolution was used.

**UV-Visible-NIR Absorption:** UV-visible-NIR absorption spectra were acquired on a JASCO V-570 spectrophotometer from 300 to 1000 nm with 0.5 nm step.

**Photoluminescence:** Photoluminescence spectra were acquired on a JASCO FP-8700 spectrophotometer. Excitation wavelength was set at 540 nm and emission was recorded from 580 to 1400 nm with a step of 1 nm and a scan speed of 100 nm min<sup>-1</sup>. For all dispersions measured the absorbance at the excitation wavelength (540 nm) was set at 0.3.

## Supporting Information

Supporting Information is available from the Wiley Online Library or from the author.

## Acknowledgements

The authors acknowledge the support provided by the ANR through the WATER-PV project N°ANR-20-CE05-0002 as well as the IRP NextPV-II, through CNRS (INC and INSIS) and RCAST/University of Tokyo. The work at LIMMS/CNRS and IIS, University of Tokyo has been partly supported by KAKENHI from JSPS (20H05660) as well as the INSIS CNRS and University of Bordeaux in the frame of the BIOMEG project. The authors thank E2S UPPA and ISIFoR for funding part of this research as well as the support from the LIGHT S&T Graduate Program (PIA3 Investment for the Future Program, ANR-17-EURE-0027) for a travel grant. The authors acknowl-

edge the technical and scientific assistance of Sydney Microscopy & Microanalysis, the University of Sydney node of Microscopy Australia. The authors further thank the support of the University of Sydney Core Research Facilities. The PolLux end station (X07DA) at the Swiss Light Source synchrotron was financed by the German Minister für Bildung und Forschung (BMBF) through contracts 05K16WED and 05K19WE2. This research used resources of the Advanced Light Source, which is a DOE Office of Science User Facility under contract no. DE-AC02-05CH11231. The authors thank support staff at the Advanced Light Source synchrotron. N.P.H. acknowledges travel funding provided by the International Synchrotron Access Program (ISAP) managed by the Australian Synchrotron, part of ANSTO, and funded by the Australian Government. N.P.H. acknowledges the University of the Tokyo Institute of Industrial Science (IIS) for funding an IIS Invited International Researcher travel grant. The authors are also grateful to Hiroshi Segawa from RCAST for the access to the photoluminescence setup and Christophe Schatz for accessing the DLS equipment.

## Conflict of Interest

The authors declare no conflict of interest.

## Data Availability Statement

The data that support the findings of this study are available from the corresponding author upon reasonable request.

## Keywords

colloidal dispersion, nanoparticles, organic photovoltaics, scanning transmission X-ray microscopy, water-based process

Received: January 25, 2023

Revised: April 17, 2023

Published online: May 17, 2023

- [1] W. Zhao, D. Qian, S. Zhang, S. Li, O. Inganäs, F. Gao, J. Hou, *Adv. Mater.* **2016**, *28*, 4734.
- [2] S. Liu, J. Yuan, W. Deng, M. Luo, Y. Xie, Q. Liang, Y. Zou, Z. He, H. Wu, Y. Cao, *Nat. Photonics* **2020**, *14*, 300.
- [3] D. Baran, T. Kirchartz, S. Wheeler, S. Dimitrov, M. Abdelsamie, J. Gorman, R. S. Ashraf, S. Holliday, A. Wadsworth, N. Gasparini, P. Kaienburg, H. Yan, A. Amassian, C. J. Brabec, J. R. Durrant, I. McCulloch, *Energy Environ. Sci.* **2016**, *9*, 3783.
- [4] D. Baran, N. Gasparini, A. Wadsworth, C. H. Tan, N. Wehbe, X. Song, Z. Hamid, W. Zhang, M. Neophytou, T. Kirchartz, C. J. Brabec, J. R. Durrant, I. McCulloch, *Nat. Commun.* **2018**, *9*, 2059.
- [5] Y. Cui, Y. Xu, H. Yao, P. Bi, L. Hong, J. Zhang, Y. Zu, T. Zhang, J. Qin, J. Ren, Z. Chen, C. He, X. Hao, Z. Wei, J. Hou, *Adv. Mater.* **2021**, *33*, 2102420.
- [6] L. Zhu, M. Zhang, J. Xu, C. Li, J. Yan, G. Zhou, W. Zhong, T. Hao, J. Song, X. Xue, Z. Zhou, R. Zeng, H. Zhu, C. C. Chen, R. C. I. MacKenzie, Y. Zou, J. Nelson, Y. Zhang, Y. Sun, F. Liu, *Nat. Mater.* **2022**, *21*, 656.
- [7] D. Yue, P. Khatav, F. You, S. B. Darling, *Energy Environ. Sci.* **2012**, *5*, 9163.
- [8] N. Espinosa, R. García-Valverde, A. Urbina, F. C. Krebs, *Sol. Energy Mater. Sol. Cells* **2011**, *95*, 1293.
- [9] S. Berry, N. Blouin, A. Distler, H.-J. Egelhaaf, M. Krompiec, A. Lohr, O. R. Lozman, G. E. Morse, L. Nanson, A. Pron, T. Sauermann, N. Seidler, S. Tierney, P. Tiwana, M. Wagner, H. Wilson, *Adv. Sci.* **2016**, *3*, 1500342.

- [10] Y. Xu, H. Yao, L. Ma, Z. Wu, Y. Cui, L. Hong, Y. Zu, J. Wang, H. Y. Woo, J. Hou, *Mater. Chem. Front.* **2021**, *5*, 893.
- [11] Y. Cui, Y. Wang, J. Bergqvist, H. Yao, Y. Xu, B. Gao, C. Yang, S. Zhang, O. Inganäs, F. Gao, J. Hou, *Nat. Energy* **2019**, *4*, 768.
- [12] J. Czolk, D. Landerer, M. Koppitz, D. Nass, A. Colsmann, *Adv. Mater. Technol.* **2016**, *1*, 1600184.
- [13] S. Qin, Z. Jia, L. Meng, C. Zhu, W. Lai, J. Zhang, W. Huang, C. Sun, B. Qiu, Y. Li, *Adv. Funct. Mater.* **2021**, *31*, 2102361.
- [14] A. Holmes, E. Deniau, C. Lartigau-Dagron, A. Bousquet, S. Chambon, N. P. Holmes, *ACS Nano* **2021**, *15*, 3927.
- [15] T. Kietzke, D. Neher, M. Kumke, R. Montenegro, K. Landfester, U. Scherf, *Macromolecules* **2004**, *37*, 4882.
- [16] T. Kietzke, D. Neher, K. Landfester, R. Montenegro, R. Guntner, U. Scherf, *Nat. Mater.* **2003**, *2*, 408.
- [17] S. Gärtner, M. Christmann, S. Sankaran, H. Röhm, E.-M. Prinz, F. Penth, A. Pütz, A. E. Türeli, B. Penth, B. Baumstümmel, A. Colsmann, *Adv. Mater.* **2014**, *26*, 6653.
- [18] T. R. Andersen, T. T. Larsen-Olsen, B. Andreasen, A. P. L. Böttiger, J. E. Carlé, M. Helgesen, E. Bundgaard, K. Norrman, J. W. Andreasen, M. Jørgensen, F. C. Krebs, *ACS Nano* **2011**, *5*, 4188.
- [19] A. Stapleton, B. Vaughan, B. Xue, E. Sesa, K. Burke, X. Zhou, G. Bryant, O. Werzer, A. Nelson, A. L. L. David Kilcoyne, L. Thomsen, E. Wanless, W. Belcher, P. Dastoor, *Sol. Energy Mater. Sol. Cells* **2012**, *102*, 114.
- [20] T. S. Gehan, M. Bag, L. a Renna, X. Shen, D. D. Algaier, P. M. Lahti, T. P. Russell, D. Venkataraman, *Nano Lett.* **2014**, *14*, 5238.
- [21] S. Ulum, N. Holmes, M. Barr, A. L. D. Kilcoyne, B. Bin Gong, X. Zhou, W. Belcher, P. Dastoor, *Nano Energy* **2013**, *2*, 897.
- [22] L. D'Olieslaeger, G. Pirotte, I. Cardinaletti, J. D'Haen, J. Manca, D. Vanderzande, W. Maes, A. Ethirajan, *Org. Electron.* **2016**, *42*, 42.
- [23] S. Ulum, N. Holmes, D. Darwis, K. Burke, a. L. D. Kilcoyne, X. Zhou, W. Belcher, P. Dastoor, *Sol. Energy Mater. Sol. Cells* **2013**, *110*, 43.
- [24] Y. J. Kim, R. D. Schaller, H. C. Fry, *Small* **2019**, *15*, 1803563.
- [25] N. P. Holmes, M. Marks, P. Kumar, R. Kroon, M. G. Barr, N. Nicolaidis, K. Feron, A. Pivrikas, A. Fahy, A. D. de Zorio Mendaza, A. L. D. Kilcoyne, C. Müller, X. Zhou, M. R. Andersson, P. C. Dastoor, W. J. Belcher, *Nano Energy* **2016**, *19*, 495.
- [26] D. Darwis, N. Holmes, D. Elkington, A. L. D. Kilcoyne, G. Bryant, X. Zhou, P. Dastoor, W. Belcher, *Sol. Energy Mater. Sol. Cells* **2014**, *121*, 99.
- [27] A. Holmes, H. Laval, M. Schmutz, S. Blanc, J. Allouche, B. Watts, G. Wantz, N. P. Holmes, K. Hirakawa, E. Deniau, S. Chambon, C. Lartigau-Dagron, A. Bousquet, *Mater. Today Chem.* **2022**, *26*, 101229.
- [28] F. Manger, K. Fischer, P. Marlow, H. Röhm, C. Sprau, A. Colsmann, *Adv. Energy Mater.* **2022**, *7*, 2202820.
- [29] C. Xie, T. Heumüller, W. Gruber, X. Tang, A. Classen, I. Schuldes, M. Bidwell, A. Späth, R. H. Fink, T. Unruh, I. McCulloch, N. Li, C. J. Brabec, *Nat. Commun.* **2018**, *9*, 5335.
- [30] C. Xie, S. Liang, G. Zhang, S. Li, *Polymers* **2022**, *14*, 4229.
- [31] M. G. Barr, S. Chambon, A. Fahy, T. W. Jones, M. A. Marcus, A. L. D. Kilcoyne, P. C. Dastoor, M. J. Griffith, N. P. Holmes, *Mater. Chem. Front.* **2021**, *5*, 2218.
- [32] C. Sun, F. Pan, H. Bin, J. Zhang, L. Xue, B. Qiu, Z. Wei, Z. Zhang, Y. Li, *Nat. Commun.* **2018**, *9*, 743.
- [33] J. Yuan, Y. Zhang, L. Zhou, G. Zhang, H. Yip, T. Lau, X. Lu, C. Zhu, H. Peng, P. A. Johnson, M. Leclerc, Y. Cao, J. Ulanski, Y. Li, Y. Zou, *Joule* **2019**, *3*, 1140.
- [34] S. Wu, *J. Polym. Sci., Part C: Polym. Symp.* **1971**, *34*, 19.
- [35] K.-H. Kim, H. Kang, H. J. Kim, P. S. Kim, S. C. Yoon, B. J. Kim, *Chem. Mater.* **2012**, *24*, 2373.
- [36] P. P. Khlyabich, A. E. Rudenko, R. A. Street, B. C. Thompson, *ACS Appl. Mater. Interfaces* **2014**, *6*, 9913.
- [37] K. Jiang, G. Zhang, G. Yang, J. Zhang, Z. Li, T. Ma, H. Hu, W. Ma, H. Ade, H. Yan, *Adv. Energy Mater.* **2018**, *8*, 1701370.
- [38] C. Xie, A. Classen, A. Späth, X. Tang, J. Min, M. Meyer, C. Zhang, N. Li, A. Osset, R. H. Fink, C. J. Brabec, *Adv. Energy Mater.* **2018**, *8*, 1702857.
- [39] K. Vandewal, A. Gadisa, W. D. Oosterbaan, S. Bertho, F. Banishoeib, I. Van Severen, L. Lutsen, T. J. Cleij, D. Vanderzande, J. V. Manca, *Adv. Funct. Mater.* **2008**, *18*, 2064.
- [40] F. Piersimoni, S. Chambon, K. Vandewal, R. Mens, T. Boonen, A. Gadisa, M. Izquierdo, S. Filippone, B. Ruttens, J. D'Haen, N. Martin, L. Lutsen, D. Vanderzande, P. Adriaensens, J. V. Manca, *J. Phys. Chem. C* **2011**, *115*, 10873.
- [41] C.-W. Chu, H. Yang, W.-J. Hou, J. Huang, G. Li, Y. Yang, *Appl. Phys. Lett.* **2008**, *92*, 103306.
- [42] B. Tan, Y. Li, M. F. Palacios, J. Therrien, M. J. Sobkowicz, *Colloids Surf., A* **2016**, *488*, 7.
- [43] J. Kosco, M. Bidwell, H. Cha, T. Martin, C. T. Howells, M. Sachs, D. H. Anjum, S. G. Lopez, L. Zou, A. Wadsworth, W. Zhang, L. Zhang, J. Tellam, R. Sougrat, F. Laquai, D. M. DeLongchamp, J. R. Durrant, I. McCulloch, *Nat. Mater.* **2020**, *19*, 559.
- [44] R. Szymanski, R. Henry, S. Stuard, U. Vongsaysy, S. Courtel, L. Vellutini, M. Bertrand, H. Ade, S. Chambon, G. Wantz, *Sol. RRL* **2020**, *4*, 2000538.
- [45] T. Zhang, M. Moser, A. D. Scaccabarozzi, H. Bristow, P. Jacquotot, A. Wadsworth, T. D. Anthopoulos, I. McCulloch, N. Gasparini, *J. Phys. Mater.* **2021**, *4*, 045001.
- [46] J. Kosco, S. Gonzalez-Carrero, C. T. Howells, T. Fei, Y. Dong, R. Sougrat, G. T. Harrison, Y. Firdaus, R. Sheelamanthula, B. Purushothaman, F. Moruzzi, W. Xu, L. Zhao, A. Basu, S. De Wolf, T. D. Anthopoulos, J. R. Durrant, I. McCulloch, *Nat. Energy* **2022**, *7*, 340.
- [47] G. Yao, Y. Ge, X. Xiao, L. Zhang, N. Yi, H. Luo, S. Yuan, W. Zhou, *ACS Appl. Energy Mater.* **2022**, *5*, 1193.
- [48] I. Persson, H. Laval, S. Chambon, G. Bonfante, K. Hirakawa, G. Wantz, B. Watts, M. A. Marcus, X. Xu, L. Ying, G. Lakhwani, M. R. Andersson, J. M. Cairney, N. P. Holmes, *Nanoscale* **2023**, *15*, 6126.
- [49] U. Flechsig, C. Quitmann, J. Raabe, M. Böge, R. Fink, H. Ade, in *AIP Conf. Proc.*, AIP, New York **2007**, pp. 505–508.
- [50] J. Raabe, G. Tzvetkov, U. Flechsig, M. Böge, A. Jaggi, B. Sarafimov, M. G. C. Vernooy, T. Huthwelker, H. Ade, D. Kilcoyne, T. Tyliščák, R. H. Fink, C. Quitmann, *Rev. Sci. Instrum.* **2008**, *79*, 113704.
- [51] X. He, B. A. Collins, B. Watts, H. Ade, C. R. McNeill, *Small* **2012**, *8*, 1920.
- [52] A. L. D. Kilcoyne, T. Tyliščák, W. F. Steele, S. Fakra, P. Hitchcock, K. Franck, E. Anderson, B. Harteneck, E. G. Rightor, G. E. Mitchell, A. P. Hitchcock, L. Yang, T. Warwick, H. Ade, *J. Synchrotron Radiat.* **2003**, *10*, 125.
- [53] B. A. Collins, H. Ade, *J. Electron Spectrosc. Relat. Phenom.* **2012**, *185*, 119.
- [54] J. Dubochet, M. Adrian, J.-J. Chang, J.-C. Homo, J. Lepault, A. W. McDowall, P. Schultz, *Q. Rev. Biophys.* **1988**, *21*, 129.